# Jupiter's low-frequency radio spectrum from Cassini/Radio and Plasma Wave Science (RPWS) absolute flux density measurements

P. Zarka and B. Cecconi

Laboratoire d'Etudes Spatiales et d'Instrumentation en Astrophysique, Observatoire de Paris, Centre National de la Recherche Scientifique, Meudon, France

W. S. Kurth

Department of Physics and Astronomy, University of Iowa, Iowa City, Iowa, USA

Received 30 September 2003; revised 5 January 2004; accepted 28 January 2004; published 14 August 2004.

[1] We apply the calibration method developed by *Dulk et al.* [2001] to the data from the Cassini/Radio and Plasma Wave Science (RPWS) High-Frequency Receiver in order to derive flux density measurements of six components of the Jovian low-frequency radio spectrum over the full frequency range of the instrument (3.5 kHz to 16.1 MHz). The estimated accuracy is better than 50%, i.e., much less than the intrinsic variations of the flux densities of these radiosources. It is mainly limited by the accuracy of the model used for the radio galactic background. Instrumental parameters such as the antennas' effective lengths and base capacitance are constrained in the calibration process. From 6 months of calibrated data centered on the Cassini-Jupiter flyby, we derive the average and peak Jovian radio spectrum between 3.5 and 16.1 MHz and its range of fluctuations, from which we deduce constraints on the beaming of the various radio components and estimate the power emitted by each component. Our calibration procedure also allows us to compare Cassini measurements of the Jovian radio spectrum with ground-based measurements performed, e.g., in Nançay above the ionospheric cutoff (10−15 MHz). It will be used to derive absolute flux measurements during the Saturn tour. *INDEX TERMS:* 6220 Planetology: Solar System Objects: Jupiter; 6954 Radio Science: Radio astronomy; 6994 Radio Science: Instruments and techniques; 2756 Magnetospheric Physics: Planetary magnetospheres (5443, 5737, 6030); 0609 Electromagnetics: Antennas; *KEYWORDS:* Jupiter, magnetosphere, radio emissions, radioastronomy, absolute flux density measurements, Cassini mission

**Citation:** Zarka, P., B. Cecconi, and W. S. Kurth (2004), Jupiter's low-frequency radio spectrum from Cassini/Radio and Plasma Wave Science (RPWS) absolute flux density measurements, *J. Geophys. Res.*, *109*, A09S15, doi:10.1029/2003JA010260.

## 1. Introduction

[2] The Cassini spacecraft en route to Saturn carries an experiment dedicated to measuring radio waves and plasma waves produced by the magnetosphere of Saturn: the Radio and Plasma Wave Science experiment (RPWS) [see *Gurnett et al.*, 2004]. This instrument also performed measurements during the flybys of Venus in 1998 and 1999 [*Gurnett et al.*, 2001], of the Earth in 1999 [*Kurth et al.*, 2001], and of Jupiter in 2000−2001. It consists of a set of receivers covering altogether the frequency range from ~0 to 16.1 MHz. These receivers are connected to seven sensors: three electric antennas, three magnetic antennas, and a Langmuir probe. The specifically "radio" part of the instrument, also called the HFR (High-Frequency Receiver), covers the range 3.5 kHz to 16.1 MHz and can be connected to the electric antennas only (there is no need for magnetic measurements as E/B = c = constant for free-space radio waves). These antennas are three wire monopoles (actually tubular booms) called here +X, −X, and Z (the names u, v, and w can also be found, as in the work of *Gurnett et al.* [2004]). Each one is 10 m long. The booms +X and −X, forming an angle of ~120°, can be used together as an electric dipole (D). The HFR has two input channels, allowing one to perform simultaneous measurements from two selectable sensors (monopole +X, −X or dipole D in channel 1 and monopole Z in channel 2). Because Cassini is not an exploratory mission like Voyager but was rather designed for in-depth studies of the Saturnian system, many experiments are programmable in a variety of operating modes optimized for specific analyses. The HFR is no exception: it can be programmed with setup parameters defining the exploration scheme of the time-frequency plane (frequency range, temporal and spectral resolutions, etc.). During the 6 month period analyzed in this paper, the HFR setup was changed at times as often as every few minutes, but at other times it could remain fixed for hours. The counterpart of this flexibility is an increased complexity of the data and of their calibration.

[3] A specific HFR setup allows one to combine simultaneous measurements from the two channels and compute autocorrelations and cross-correlations between the corres-


0148-0227/04/2003JA010260$09.00

ponding signals, providing thus the capability to derive the full polarization (four Stokes parameters S = flux, U, Q = linear polarization, and V = circular polarization) and **k** vector (characterized by an azimuth angle $\varphi$ and an elevation angle $\theta$) of the incoming radio waves: this is the "direction-finding" mode of the instrument which allows one to restore an angular resolution about 1°–2° [*Ladreiter et al.*, 1995; *Vogl et al.*, 2004]. However, the flux S intervenes here as a multiplying (scaling) factor on the measurements of all sensors, which implies that its accurate determination has to be carried out separately.

[4] The present paper describes the method that has been implemented on the data from the Cassini/RPWS HFR in order to derive absolute flux density measurements in routine with this receiver over its full frequency range, independent of its mode of operation and of the sensors used (monopole or dipole). It is then applied to 6 months of data around Cassini's closest approach to Jupiter (30 December 2000), in order to obtain accurate measurement of the full Jovian low-frequency radio spectrum, which includes at least seven distinct radio components. The interest of absolute flux density measurements is obvious to constrain emission mechanisms, perform radio energy budgets (to be correlated with various input powers on the magnetosphere [see *Zarka et al.*, 2001b]), and derive unbiased long series of flux measurements. The latter allow one to compare the energetics of the various radio components at all the visited planets as well as to correlate with solar wind fluctuations or other possible "control" parameters of the radio emissions [see *Zarka*, 1998, and references therein]. This capability will be particularly useful during the Saturn tour starting mid-2004. Applied to Jupiter, it also allows us to intercompare various ground-based and space-based observations of Jupiter's radio emissions.

## 2. Method

### 2.1. Short Antenna Calibration

[5] When the length of a wire antenna is short as compared to the wavelength (2L significantly less than $\lambda/2$, where $\lambda$ is the radio wavelength and L is the wire length), the antenna sees an homogeneous time-varying electric field and thus the conversion of the signal P (in $V^2$ $Hz^{-1}$) measured at the receiver's input into incoming flux density S (in $Wm^{-2}$ $Hz^{-1}$) can be simply written [*Manning*, 2000]:

$$S = \frac{P}{Z_o L^2 \left(\frac{c_a}{c_a + c_b}\right)^2}, \qquad (1)$$

where $Z_o$ is the impedance of free space ($Z_o = (\mu_o/\varepsilon_o)^{1/2} = 120\pi = 377\ \Omega$), L is the effective length of the antenna, $c_a$ is the antenna capacitance, and $c_b$ is the base capacitance of the antenna mount and feed. Values of P are derived from output data numbers returned by the HFR after a "zero level" calibration step (described by *Manning* [1999]) correcting for the specific setup of the instrument (temporal and spectral resolutions, etc.).

[6] The accuracy associated to equation (1) is linked to that on L, $c_a$, and $c_b$. The geometrical center-to-center distance of +X and −X booms, 9.26 m (cf. RPWS antenna calibration document, University of Iowa, available at http://www-pw.physics.uiowa.edu/~wsk/cas/daspage/antenna.pdf), is a good approximation of the effective length of the electric dipole D. The effective length of the monopoles is modified by the presence of the spacecraft body. The antenna capacitance, $c_a \sim 100$ pF for the monopoles, can be reliably computed theoretically [*Manning*, 2000]. The base capacitance $c_b$ is more difficult to estimate due to its dependence on the antenna mechanism, cables, HFR input, and spacecraft structure. Computation using an antenna modeling program with an accurate representation of the geometry yielded $c_b \sim 150$ pF for the monopoles (both capacitance should be halved for dipole measurements) so that $c_a/(c_a + c_b) \sim 0.4$. This capacitance ratio plays thus the role of a ~8 dB attenuator for HFR measurements.

[7] Short antenna calibration is the standard method to derive absolute flux densities at low frequencies with a reasonable accuracy (a few tens of %) depending on the knowledge of L and of $c_a/(c_a + c_b)$. It is valid as long as $2L \ll \lambda/2$, i.e., $f \ll 8$ MHz. We will see below that the actual limit on Cassini is in practice $f \leq 2$ MHz. Above this frequency, $c_a$ increases (up to $\sim\infty$ at half-wave resonance), and substantial error is made using equation (1), increasing with increasing frequency. We must then use another calibration procedure at higher frequencies.

### 2.2. Calibration Using the Galaxy

[8] Because the background radio radiation of the galaxy largely dominates the instrumental noise above ~1 MHz (up to several hundreds of MHz) and thanks to the good sensitivity of the receiver, the HFR is able to detect the galactic background permanently, unless it is hidden by intense, sporadic superimposed emission from Jupiter or the Sun. The galactic background at low frequencies (≈1–100 MHz) is known well enough to play the role of a calibration source. This is especially true when using monopole or dipole antennas, which have a very large primary beam ($8\pi/3$) and thus smooth out the weak spatial fluctuations of the galactic emission.

[9] *Dulk et al.* [2001] built an empirical analytical galactic background model based on >100 independent measurements from >20 observers (including ISEE 3, Wind/WAVES, Ulysses, BIRS, etc.) between ~0.5 and 20 MHz. The galactic background flux density $S_g$ (in $Wm^{-2}$ $Hz^{-1}$) detected in a dipole's beam thus is

$$S_g = \left[ I_g \ f^{-0.52} \left( \frac{1 - e^{-\tau}}{\tau} \right) + I_{eg} \ f^{-0.8} e^{-\tau} \right] \times \Omega \times \eta, \qquad (2)$$

where $I_g = 2.48 \times 10^{-20}$ is the galactic contribution, $I_{eg} = 1.06 \times 10^{-20}$ is the extragalactic contribution, $\tau(f) = 5.0 \times f^{-2.1}$ is the interstellar opacity, f is the frequency in MHz, $\Omega = 8\pi/3$ is the dipole beam, and $\eta(f)$ is a geometrical correction factor for the inhomogeneous distribution of the background radio radiation between the galactic plane and the galactic poles ($\eta = 1$ for $f \leq 3$ MHz, and it increases by ~4.3%/MHz for $f > 3$ MHz).

[10] In addition, *Manning and Dulk* [2001] compiled measurements of the brightness temperature $T_B$ of the galactic background between 200 kHz and 13 MHz with the Wind/WAVES experiment. Once converted to flux densities ($S = 2kT_B\Omega/\lambda^2$), these tabulated measurements are in perfect agreement with the above model above 500 kHz and allow us to extend it down to 200 kHz.

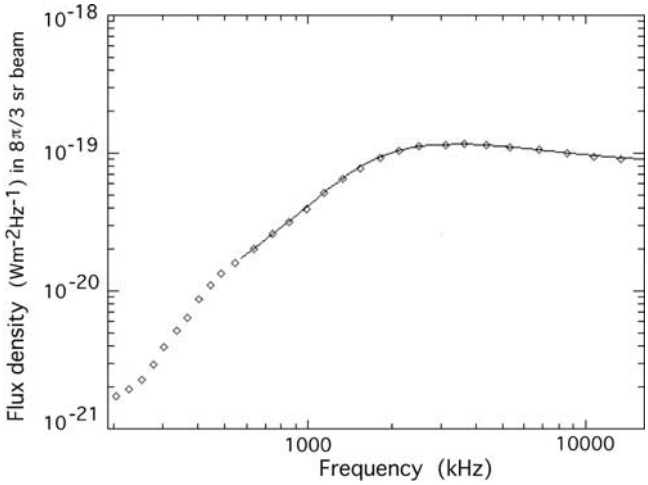


**Figure 1.** Galactic low-frequency model radio spectrum Sg(f) derived from *Dulk et al.* [2001] (continuous line) and *Manning and Dulk* [2001] (diamonds). Their combination is our reference galactic background flux density spectrum.

[11] For the purpose of the present work, we combined the results from these two papers in a single reference galactic background flux density spectrum tabulated between 200 kHz and 16.1 MHz. This galactic low-frequency radio spectrum $S_g(f)$ is displayed in Figure 1. Conversion of the signal (P) measured at the receiver's input into incoming flux density (S) now is

$$S = \frac{P - P_g - P_r}{P_g} S_g, \tag{3}$$

with $P_g(f)$ corresponding to the measured galactic background spectrum and $P_r(f)$ corresponding to the receiver noise level.

### 2.3. Receiver Noise

[12] Measurements of $P_r$ performed on the ground before launch are polluted by the electromagnetic environment of the laboratory. Therefore 1 hour of observation with RPWS was carried out 10 days after launch at instrument turn-on (25 October 1997, 0000 to 0100 UT) before deploying the antennas. A series of 119 spectra covering the full spectral range of the instrument were recorded in both HFR channels, connected to the undeployed dipole D and monopole Z, respectively. Figure 2a displays the corresponding dynamic spectrum from channel 1. Only background noise and weak interference lines were detected. The latter are attributed to various onboard activity and should thus not be included in the receiver's noise level $P_r$ that we will use as a reference. We obtained $P_r$ by recording the minimum level detected at each frequency during this 1-hour interval and then removing discrete interference lines (with linear interpolation through them). The corresponding noise levels for the two channels are displayed on Figure 2b Several remarks can be made: (1) the noise level is higher by 1−2 dB in channel 1 (input of dipole D); (2) the minimum noise level corresponds to $\approx$7−10 nV $Hz^{-1/2}$, consistent with expectations from the laboratory; (3) the level increases toward the lower end of each HFR subband (spectral analysis is performed through digital filtering plus automatic gain control loop in the range 3.5−320 kHz and with a swept frequency filter, heterodyne scheme, above $\sim$300 kHz).

[13] The discontinuity about 300 kHz is attributed to the change of subband, implying the use of different parts of the receiver's electronics. The increase at very low frequencies (<10 kHz) may be attributed to 1/f noise as well as noise generated by spacecraft subsystems (EMI is electromagnetic interference). In both cases, it should be included in $P_r$. The increase between $\sim$1 MHz and 300kHz may be attributed either to noise generated by spacecraft subsystems or to external noise picked up even

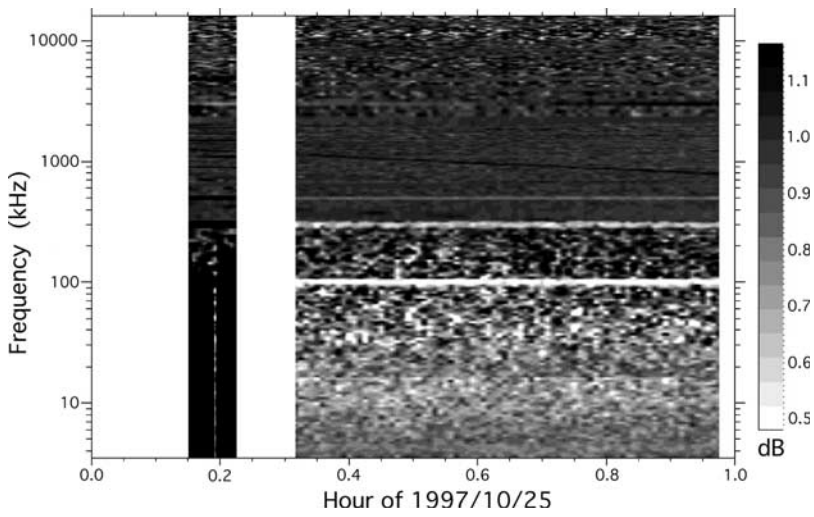


**Figure 2a.** Dynamic spectrum of the receiver's output in HFR channel 1 before deployment of the dipole antenna. Background noise fluctuations and weak interference lines are detected.

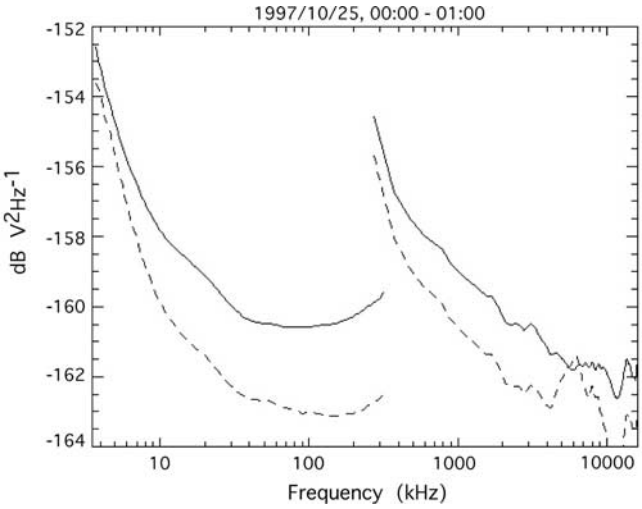


**Figure 2b.** Minimum noise levels measured before antenna deployment at the inputs of channel 1 (dipole D shown by continuous lines) and channel 2 (monopole Z shown by dashed lines) in the two HFR subbands (3.5–320 kHz and ~300–16100 kHz).

in the absence of deployed antennas (as suggested also by remark 1). Only the former should be included in $P_r$, because external noise varies with the plasma environment of the spacecraft. We propose a solution for this issue in section 2.5.

### 2.4. Measured Galactic Noise

[14] The observed HFR spectrum corresponding to the sum of galactic background noise and receiver noise ($P_g + P_r$) was derived as follows:

[15] 1. Several intervals of a few hours were selected, all with a very low level of solar and planetary radio activity and a low level of spacecraft interference; these data were recorded with various instrument setups. Figure 3a displays one such interval where the dynamic spectrum reveals a quiet galactic radio background with a few solar type III bursts superimposed [see, e.g., *Bougeret et al.*, 1998; *Robinson and Cairns*, 2000];

[16] 2. At each frequency, the statistical fluctuations of the background level appear as a well-defined gaussian distribution centered on the average value of ($P_g + P_r$) at that frequency, as illustrated in Figures 3b and 3c.

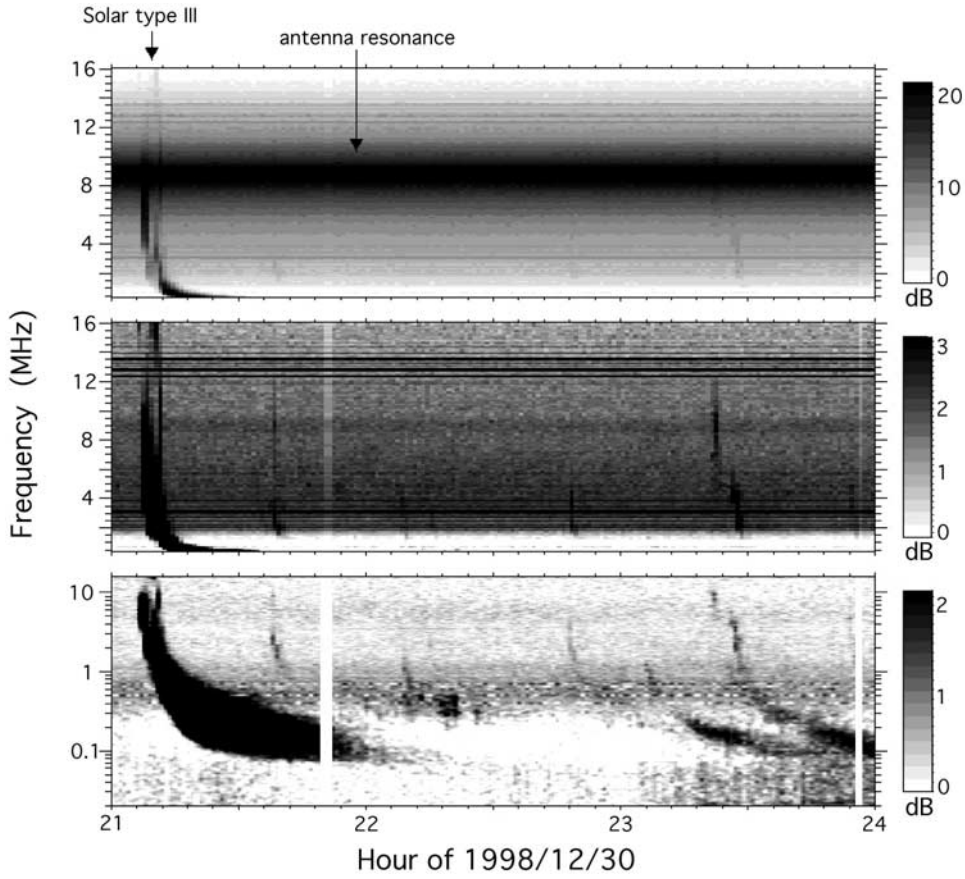


**Figure 3a.** Quiet interval of HFR data recorded with the dipole antenna (channel 1). Top panel displays raw data with linear frequency scale. Middle panel displays the dynamic spectrum after subtraction of a frequency-dependent background. Bottom panel shows the whole HFR band after background subtraction, with log frequency scale. One intense and several weak solar type III bursts are detected.

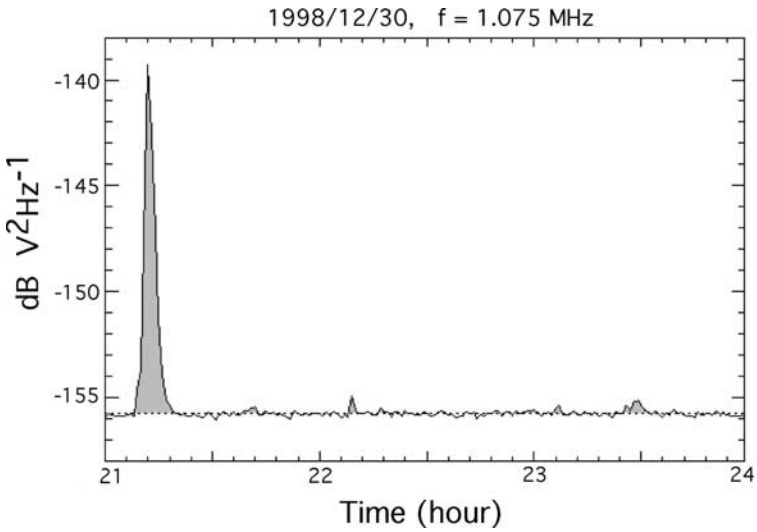


**Figure 3b.** Cut of Figure 3a at frequency f∼1 MHz. Time resolution is 60 s per sample. Type III emission is gray shaded. The background level is indicated by the dotted line. Its fluctuations are less than ±0.2 dB.

[17] It was found that the zero level calibration step (through which HFR data numbers are converted to $V^2$ $Hz^{-1}$) corrects for the changing instrument setups with a relative accuracy better than 1–2 dB. Conversely, the dipole and monopole antennas (furthermore perturbed by the large spacecraft body) have very different spectral responses. Measurements performed with dipole and monopole antennas should then be processed separately. Figures 4a and 4b accordingly display the resulting curves $(P_g + P_r)(f)$ for measurements performed respectively with the dipole antenna and with ±X monopole antennas (similar curves are obtained for +X or −X separately).

[18] The galactic background noise spectrum derived in this way is found to be very stable in time when

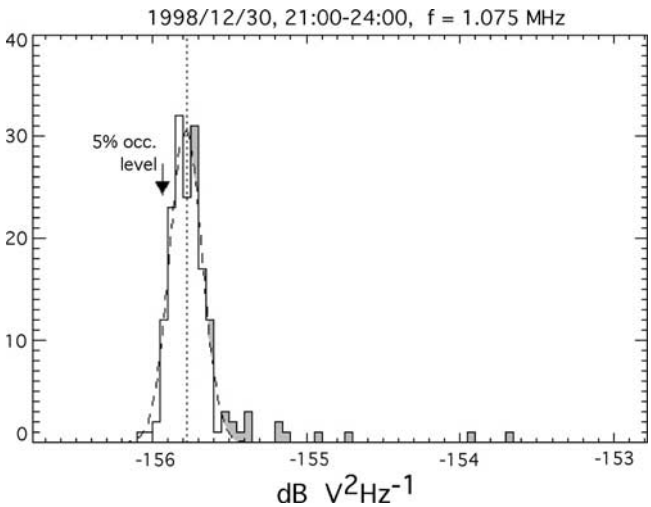


**Figure 3c.** Histogram of intensities in 60 s samples of Figure 3b, at f = 1.075 MHz. The gaussian distribution (dashed) corresponds to the galactic noise plus receiver noise and their fluctuations at this frequency. The average value of (Pg + Pr) at 1.075 MHz corresponds well to the mode of the histogram (dotted line). The higher intensity tail (gray shaded) corresponds to measurements of the type III emission. The limit of the lower 5% occurrence level is arrowed.

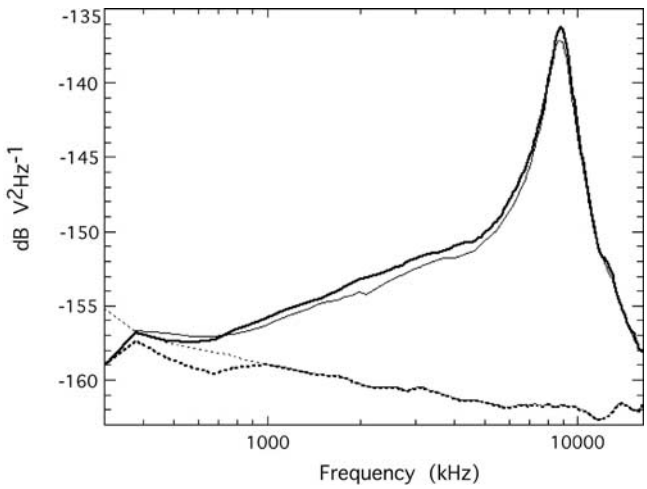


**Figure 4a.** Galactic background noise spectrum (plus receiver noise) measured by the HFR with the dipole antenna (channel 1). The peak at 8.8 MHz is the electrical resonance at $2L \approx \lambda/2$. The lightface continuous curve was obtained from quiet intervals of a few hours far from Jupiter. The boldface continuous curve, computed as the lower 5% occurrence level detected at each frequency during a 6-month interval centered on the Jupiter flyby, serves as our reference for (Pg + Pr)(f) for Jupiter studies. The lightface dotted curve is the minimum noise level measured before antenna deployment at the input of channel 1 (taken from Figure 2b). The boldface dotted line is the receiver noise spectrum in dipole mode as derived in section 2.5.

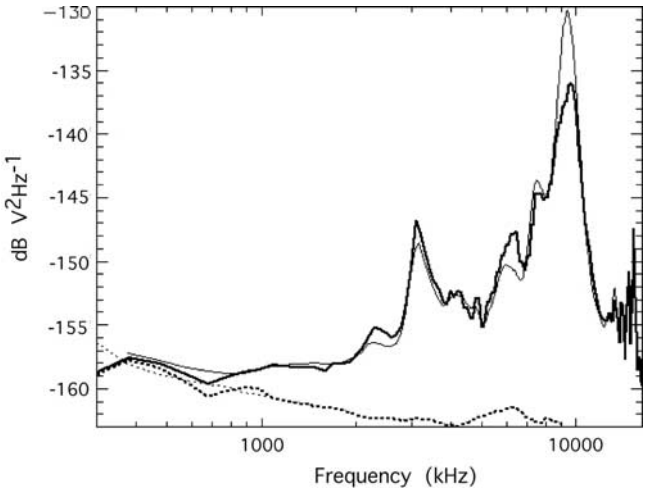


**Figure 4b.** Galactic background noise spectrum (plus receiver noise) measured by the HFR with the ± X monopole antennas (channel 1). The main electrical resonance is at 9.4–9.6 MHz. Peaks at 3 MHz and ≥13 MHz are interference. The lightface continuous curve was obtained from quiet intervals of a few hours far from Jupiter. The boldface continuous curve, computed as the lower 5% occurrence level detected at each frequency during a 6-month interval centered on the Jupiter flyby, serves as our reference for (Pg + Pr)(f) for Jupiter studies. The lightface dotted curve is the minimum noise level measured before antenna deployment at the input of channel 2 (taken from Figure 2b). The boldface dotted line is the receiver noise spectrum in monopole mode as derived in section 2.5.

measured with the dipole antenna (Figure 4a). The main electrical resonance at 8.8 MHz corresponds to the imaginary part of the antenna impedance becoming inductive and equal to $-c_b$, just above the frequency at which $2L \approx \lambda/2$ [*Manning*, 2000]. For measurements with monopole antennas (Figure 4b) the main electrical resonance is about 9.5 MHz and secondary peaks appear on the measured galactic spectrum. Some of them (at 3 MHz and above 13 MHz) are due to quasi-permanent spacecraft interference (which cancel out in dipole mode), others (at ~6.3 and 7.5 MHz) are secondary electrical resonances resulting from the interaction between the antenna and the conductive spacecraft structure, especially the 13-m-long magnetometer boom placed symmetrically between the +X and −X monopoles. In monopole mode, the resonance frequency is found to vary with time (between 9.4 and 9.6 MHz for the main one) and in amplitude (by a few dB), probably due to moving parts on the spacecraft (as the Cosmic Dust Analyzer and soon the Huygens probe). This may be a major limitation on the accuracy of the calibration using the galaxy (equation (3)). The internal HFR calibrations periodically carried out in-flight do not help in this case because the problem arises from the variation of the antenna response.

[19] In order to achieve better accuracy, it is thus necessary to compute the galactic spectrum measured at the time of the observations we want to calibrate. During the ±6 months around Jupiter's flyby, the nearly continuous Jovian radio activity does not leave room for quiet intervals of a few hours. However, we noticed that the limit of the lower 5% occurrence level in histograms such as in Figure 3c, which takes advantages of quiet periods frequency per frequency and independent of their duration, is always close (within 1 dB) of the galactic background level. Thus we computed in this way the galactic spectrum measured during the Jupiter flyby, which is displayed on Figures 4a and 4b (boldface continuous lines). These plots confirm that little change is observed in dipole mode but significant variations in monopole mode near the resonances. In the following, we will use these latter spectra as reference for $(P_g + P_r)(f)$.

### 2.5. Comparison and Merging of the Two Calibration Methods

[20] Calibration using the short antenna formula in equation (1) is valid for $2L \ll \lambda/2$, i.e., $f \ll 8$ MHz. As said above, it will be used in practice up to 2 MHz. The formula in equation (1) has to be modified as follows to include subtraction of receiver noise:

$$S_1(f) = \frac{P(f) - P_r(f)}{K}, \tag{4}$$

with P in $V^2\ Hz^{-1}$ and

$$K = Z_o L^2 \left(\frac{c_a}{c_a + c_b}\right)^2. \tag{5}$$

K has to be determined accurately and should be different for dipole and monopole measurements (cf. section 2.1).

[21] Conversely, calibration using the galactic background as a reference (equation (3)) requires that the latter is known with good accuracy. This is the case only above 200 kHz (Figure 1), but in practice we will only use measurements from the HFR subband starting at $f \sim 300$ kHz. Leaving subtraction of the galactic background as a last step, we have thus:

$$S_2(f) = \frac{P(f) - P_r(f)}{P_g(f)} S_g(f). \tag{6}$$

A difficulty is raised by the determination of $P_r$ at low frequencies. The predeployment noise levels of Figure 2 are not small compared with P and $P_g$ in the range 0.3–1 MHz: the difference between $(P_g + P_r)$ and these noise levels is <3 dB in that range as displayed in Figures 4a and 4b and even negative at 300 kHz, suggesting that predeployment noise levels include external noises and are an overestimation of $P_r$.

[22] Determination of K and of $P_r$ was performed as follows:

[23] 1. Comparing $S_1(f)$ and $S_2(f)$ in the range 1–2 MHz, where both calibration methods are reliable, we find that $S_2(f)/S_1(f) = KS_g(f)/P_g(f)$ is independent of f, as expected; above 1 MHz, $P_g$ can be determined with an error ≤1 dB as $(P_g + P_r)$ minus the pre-deployment noise levels (Figures 4a and 4b). The condition $S_2(f)/S_1(f) = 1$ then allows us to determine K; we find $K = 3520\ \Omega m^2$ in dipole mode and $K = 1070\ \Omega m^2$ in monopole mode. We discuss in the next section

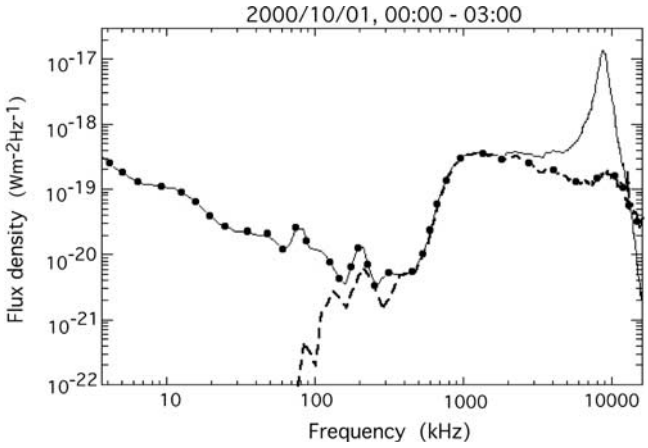


**Figure 5a.** Average spectrum of Jovian radio emissions detected on 2000/10/01, 0000 to 0300 with the HFR dipole antenna. Distance to Jupiter is 1184 $R_J$ or 0.565 AU. Spectra obtained through short dipole calibration (continuous line) and calibration based on the galactic background (dashed line) are compared (see text). Final (composite) calibrated spectrum is indicated by solid dots.

the consequences of these results in terms of antenna parameters.

[24] 2. In the range 0.3–1 MHz, we must also have $S_2(f)/S_1(f) = 1$ with the same values of K; considering $(P_g + P_r)$ as reliable, we can deduced $P_r$ as $P_r(f) = (P_g + P_r)(f) - KS_g(f)$. The resulting curve $P_r(f)$ is displayed in Figures 4a and 4b (boldface dotted lines) for dipole and monopole measurements; the receiver noise determined in this way does not exceed $-158$ dB $V^2$ $Hz^{-1}$, i.e., $\sim$13 nV $Hz^{-1/2}$, again consistent with laboratory estimates.

[25] Finally, calibration of measurements over the whole HFR band (3.5 kHz to 16.1 MHz) was performed as follows: (1) below 1 MHz using short dipole calibration only; (2) between 1 and 2 MHz by averaging the results of both calibration methods; (3) above 2 MHz using the reference galactic background only. Then, the galactic background spectrum of Figure 1 is subtracted from calibrated data, and a correction is applied for the variable Cassini-Jupiter distance (flux densities are normalized to a distance of 1 AU).

[26] Figures 5a and 5b illustrate this procedure: the data correspond to the interval from 0000 to 0300 on 1 October 2000 (DOY 275). Measurements were performed with the dipole antenna. Distance to Jupiter was 1184 $R_J$ (Jovian radius – 1 $R_J$ = 71400 km) or 0.565 AU. Strong Jovian radio emission was detected in the hecto-decameter range and weaker one in the kilometer range. Figure 5a compares the flux density spectrum averaged over the 3-hour period obtained via both calibration methods over the whole frequency range. The two methods match perfectly in the range 0.3–2 MHz. Above 2 MHz, the short antenna calibration (continuous line) increasingly overestimates the flux density up to almost two orders of magnitude at antenna resonance. In contrast, the latter is smoothed out via calibration using the galactic background (dashed line). Below 200 kHz, extrapolation of the galactic background is not reliable so that corresponding flux densities are meaningless. The final calibrated flux density spectrum is thus composite from the two methods: short antenna calibration below 2 MHz and calibration via galactic background above

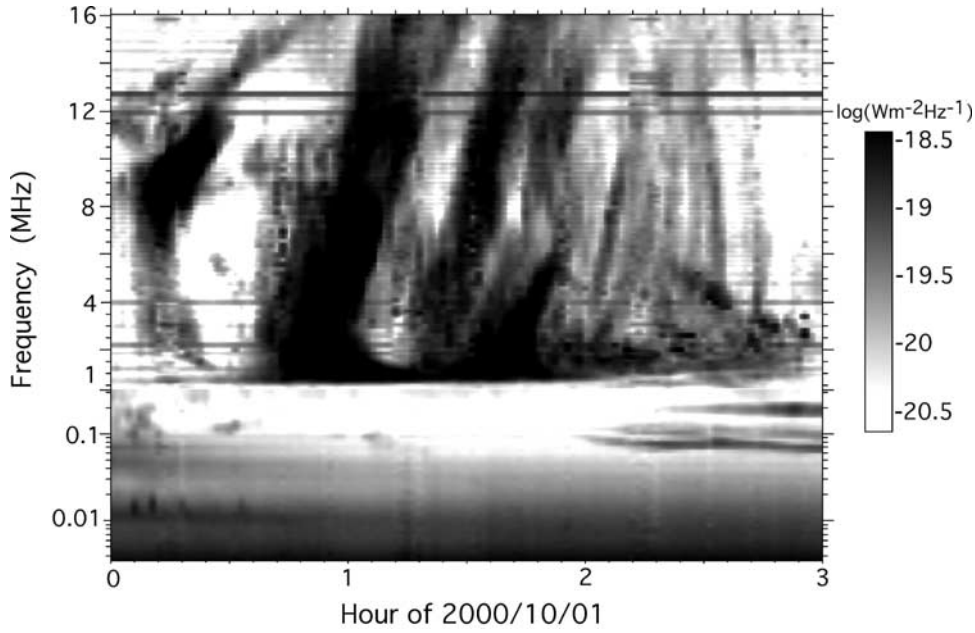


**Figure 5b.** Dynamic spectrum of received Jovian flux densities, normalized to a distance of 1 AU. Time integration is 90 s per spectrum. The low-frequency scale ($f \leq 320$ kHz) has a log scale with spectral resolution $\delta f/f = 10\%$. The high-frequency scale ($\geq$320 kHz) is linear with spectral resolution $\delta f$ = 100 kHz. Strong hecto-decameter emissions (so-called radio arcs) is prominent above $\sim$1 MHz, together with weaker patches of kilometer emission about 100–200 kHz. Local plasma frequency at the spacecraft is below 10 kHz.

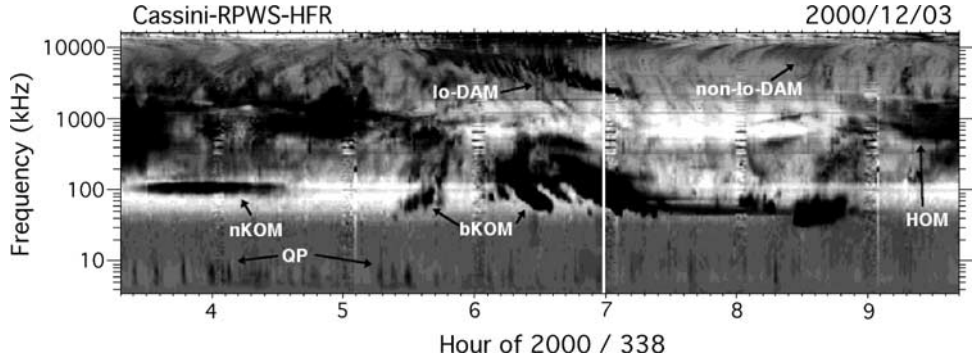


**Figure 6a.** Jovian low-frequency radio emissions detected on 3 December 2000 by the RPWS experiment onboard Cassini approaching Jupiter. Frequency range is 3.5 kHz to 16.1 MHz. The Io-DAM emission appears here down to about 2 MHz, while weaker Io-independent (non-Io-DAM) arcs merge with the hectometer component (HOM) detected down to ~400 kHz. The auroral broadband kilometer component (bKOM) is detected down to ~40 kHz. The narrowband emission (nKOM) about 100 kHz is generated at or near the plasma frequency $f_{pe}$ in Io's torus. The quasi-periodic (QP) bursts, spaced by 5 to >15 min, are detected in the ~5 to 20 kHz range. Distance to Jupiter was 383 $R_J$ ($2.7 \times 10^7$ km) at the time of this observation.

1 MHz (dotted). Figure 5b displays a dynamic spectrum calibrated accordingly. It should also be noted that the lower-frequency end of the spectrum, below a few tens of kHz, partly consists of local noise (quasi-thermal noise, electrostatic noise due to photoelectrons and various other electrostatic and electromagnetic noises [see *Zarka*, 2004, and references therein]). Levels in $Wm^{-2}\ Hz^{-1}$ are meaningless for most of them, and furthermore they are corrupted by the correction for the distance to Jupiter. The spectra and dynamic spectra we obtain following the above procedure apply thus only to Jovian radio emissions (with f necessarily above the local plasma frequency ~5–10 kHz). Before applying our calibration procedure to the Jupiter flyby data set, we briefly comment below on the consequences that our results imply on antenna parameters (effective lengths and capacitance).

## 3. Constraints on Antenna Parameters

[27] The above values deduced for $K = Z_o L^2 c_a^2/(c_a + c_b)^2$ imply $Lc_a/(c_a + c_b) = 3.06$ m in dipole mode and 1.68 m in monopole mode. The electrical resonance at 8.8 MHz (dipole case) (cf. section 2.4) implies an effective length $L_D \geq 8.5$ m, consistent with the geometrical estimate of section 2.1. This leads to $c_a/(c_a + c_b) \leq 0.36$. With $c_a$ = 50 pF, one gets $c_b \geq 89$ pF, larger than half the computed monopole value.

[28] For the ±X monopoles, resonance about 9.5 MHz implies an effective length $L_M = 7.9$ m (note that in this case, $L = L_M/2 \approx 4$ m must be used in the expression of K because the voltage is measured between the monopole and the spacecraft). This leads to $c_a/(c_a + c_b) \leq 0.42$. With $c_a$ = 100 pF, one gets $c_b \geq 138$ pF, consistent with estimates of section 2.1.

[29] The effective length inferred for ±X monopole antennas is consistent with that obtained through a rheometric study of a Cassini model [*Rucker et al.*, 1996] (which also gives values for $L_M/2$). For the dipole, the length deduced from the resonance is 15% higher than that obtained from rheometric measurements (7.3 m). It should, however, be noted that rheometry is more efficient for determining the orientation of the antennas (identifying the zeros and relative maxima of the antenna response) rather than their effective length (which depends on the absolute value of the measured signals).

[30] Rheometry also suggested $L_Z/L_{\pm X} = 1.1$, while resonances are observed at the same frequencies, suggesting a ratio closer to 1. Finally, calibration of the RPWS direction-finding mode using Jupiter as a radiosource of reference implies a ratio $L'(Z)/L'(\pm X)$ about 0.85 [*Vogl et al.*, 2004], with $L' = L(c_a/c_a + c_b)$. Assuming identical antenna capacitance, this implies a larger base capacitance (~180 pF) for the Z monopole than for the ±X ones.

## 4. Jovian Radio Spectrum

### 4.1. Jovian Radio Components

[31] Jupiter's low-frequency radio spectrum consists of at least seven main components [see e.g., *Zarka*, 2000]. Those are, by increasing frequency, (1) the nonthermal continuum (NTC), a featureless smooth low-frequency radiation partly trapped in and partly escaping the magnetospheric cavity [*Kurth*, 1992]; (2) the quasi-periodic (QP) bursts associated with part of the escaping NTC [*MacDowall et al.*, 1993; *Kaiser*, 1998]; (3) the narrowband kilometric radiation (nKOM) originating from Io's plasma torus [*Reiner et al.*, 1993]; (4) the broadband kilometric radiation (bKOM) of very high latitude auroral origin [*Ladreiter et al.*, 1994]; (5) the hectometer emission (HOM), originating from high-latitude field lines threading the outer parts of the Io torus [*Ladreiter et al.*, 1994; *Zarka et al.*, 2001a]; (6) the auroral decameter emission, whose high-latitude source is not precisely located (it is often noted non-Io-DAM to distinguish it from the following component); (7) the Io-dependent decameter emission (Io-DAM), produced along field lines threading Io's dense plasma wake [*Zarka et al.*, 2001a].

[32] Figure 6a displays a dynamic spectrum recorded by Cassini/RPWS on DOY 338 of year 2000, before closest approach. All the Jovian radio components except the NTC show up on this figure, revealing a complex morphology in

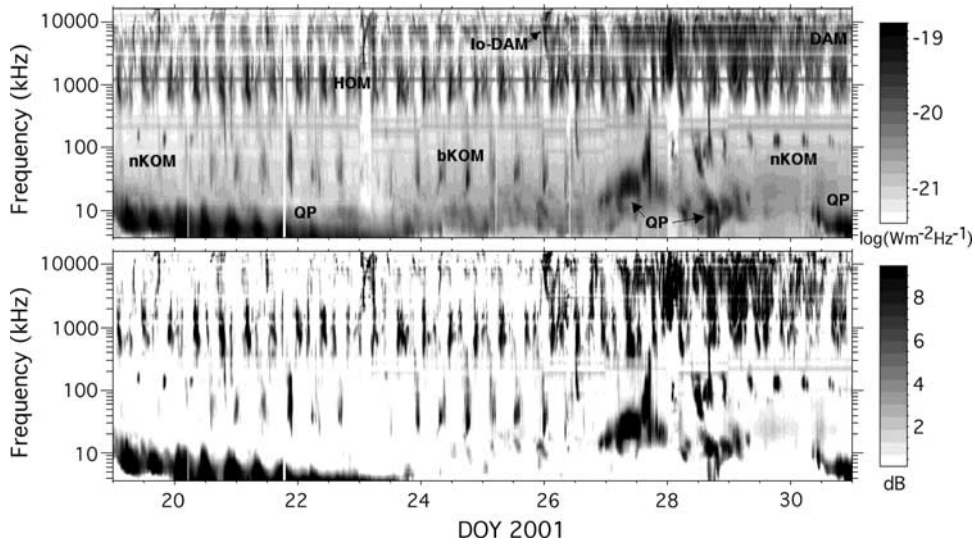


**Figure 6b.** Long-term dynamic spectra of Jovian radio components over a 12-day interval after closest approach. The upper panel displays calibrated flux densities as measured by Cassini, from a distance of 292 to 436 $R_J$ from Jupiter. The bottom panel displays the same data after subtraction of a frequency-dependent background leading to enhancement of the contrast of long-term variations of the various components. The variable spectral range and strong modulation of QP emissions by the planetary rotation are well visible, as well the strong increase in DAM activity about DOY 27.

the time-frequency plane, as well as partly overlapping spectral ranges.

[33] As the trapped component has frequencies lower than the plasma frequency $f_{pe}$ in the magnetosheath, it was observed only for a few hours on 2 days of the Cassini-Jupiter encounter period. It will not be studied here. The escaping NTC reaches frequencies higher than $f_{pe}$ (magnetosheath) and can thus escape in the solar wind. It is produced in narrow frequency bands at magnetospheric boundaries and spreads into a continuum due to multiple reflections with random Doppler shifts in the magnetospheric cavity. It merges with intense QP bursts tails from which it is difficult to distinguish. In the present paper we have chosen to restrict our very low frequency studies to the QP bursts tail, and thus we will not address escaping NTC as a separate component.

[34] A set of RPWS-HFR data calibrated according to the procedure described above has been created for the period from 1 October 2000 to 1 April 2001, i.e., 182 days with almost continuous coverage (data gaps represent ~10% of the total, including a large gap between 1 and 5 February 2001) during which Cassini was within 1200 $R_J$ from Jupiter (0.57 AU). Cassini had a near-equatorial trajectory, with a magnetic latitude ranging from $-8°$ to $+13°$ before closest approach and from $-13°$ to $+6°$ after closest approach. Time resolution is 90 s per spectrum. It was chosen as a best compromise between all the setups used over the Jupiter flyby, but data at higher time resolution (down to ~10 s/spectrum) do exist during limited intervals. However, in the present paper we do not draw any conclusion about fluctuations shorter than 90 s. The frequency range used over the whole periods consists of 48 logarithmically spaced channels between 3.5 and 320 kHz (with $\delta f/f = 10\%$), followed by 158 linearly spaced channels (with $\delta f = 100$ kHz) between 375 and 16,075 kHz. Here 88.5% of the data have been recorded in monopole mode, 5.5% have been recorded in dipole mode, and 6% have been recorded in a combination of both (monopole below 2 MHz, dipole above).

[35] This set of calibrated HFR data allows us to create long-term dynamic spectra, such as Figure 6b, whose examination immediately reveals interesting properties of the various components, as for example, the following:

[36] 1. QP bursts exhibit a variable low-frequency cutoff apparently related to magnetospheric compressions [see *Gurnett et al.*, 2002]. The bursts, not individually resolved here, have extended low-frequency tails probably due to propagation delays, which superimpose and merge to produce at least part of the escaping continuum radiation [*Desch*, 1994; *Kaiser*, 1998]. Propagation effects affecting similar bursts in the Earth's magnetosphere have been studied in details by *Steinberg et al.* [2004]. Figure 6b reveals a strong modulation of QP emissions by the planetary rotation with one peak per rotation, consistent with earlier results [*MacDowall et al.*, 1993; *Kaiser et al.*, 1993]. These bursts have been mostly detected from the dusk and nightside of Jupiter during the flyby [*Hospodarsky et al.*, 2004]. Their source appears modulated in a clock-like way, illuminating simultaneously a broad solid angle, rather than rotating with the planet.

[37] 2. Here nKOM appears in episodes as first noted by *Louarn et al.* [1998], but the correlation of nKOM activity with auroral (HOM and DAM) radio activity is not straightforward.

[38] 3. Here bKOM appears extremely sporadic. It experiences long-term activity variations in addition to rotation modulation and shows a broad variable spectral range. Its long-term variations do not seem correlated with those nKOM, HOM, or DAM. Its rotation modulation is consistent with a lighthouse-like beam, with two peaks per rotation

**Table 1.** Typical Spectral Range of Jovian Low-Frequency Radio Components (Except NTC)

| Spectral Range, kHz | Name of Component |
|---|---|
| 3.5–23[a] | QP |
| 60–160 | nKOM |
| 23–400 | bKOM |
| 400–3000 | HOM |
| 3000–>16,100[b] | DAM |

[a]Value is ≤10 kHz when magnetosphere is dilated and ≥10 kHz when it is compressed.
[b]Including auroral (non-Io) component as well as Io-dependent component.

about 40° and 190° longitude (these peaks may be due to the intersection of the opposite walls of a widely open rotating hollow cone with the observer's direction).

[39] 4. HOM is rotation modulated in the same way as bKOM but in antiphase, with peaks about 100° and 290° longitude [see, e.g., *Lecacheux et al.*, 1992]. It clearly merges with higher-frequency emission (non-Io-DAM) occurring simultaneously at the same phase of the planetary rotation (see, e.g., DOY 27–31 in Figure 6b). This strongly supports the interpretation of HOM and non-Io-DAM as the low-frequency and high-frequency part of the same radio component, respectively. On another hand, part of the time HOM emission is detected with much higher intensity than non-Io-DAM (see, e.g., DOY 19–26 in Figure 6b).

[40] 5. By contrast, Io-DAM appears as relatively isolated "arcs" in the high-frequency part of the dynamic spectra (see, e.g., DOY 19, 21, 23, 26), with a low-frequency cutoff between 2 and 2.5 MHz and thus disconnected from HOM emission. Non-Io-DAM emission appears often as intense as Io-DAM, except at frequencies ≥8 MHz (see below). The systematic study of modulations and long-term temporal variations of Jovian radio components will be the subject of a further paper.

### 4.2. Jovian Low-Frequency Radio Spectrum

[41] Obtaining a composite spectrum showing representative flux densities for all the studied Jovian low-frequency radio components is not a simple task: all these components display large intensity variations at several timescales; not all components show similar long-term variations; some components partly superimpose over a common frequency range, but have uncorrelated time variations; occasional presence of intense Solar type III bursts across a large part of the HFR spectral range pollute the computation of average spectra; components with a low duty cycle (as, e.g., bKOM) are diluted by time-averaging.

[42] The solution we have found to overcome this difficulties consists in:

[43] 1. Visual inspection of dynamic spectra over the whole 182-day interval of calibrated RPWS-HFR measurements for identifying periods of activity (at weak, moderate, or high level) for each radio component independently.

[44] 2. Selection of time intervals before and after Cassini-Jupiter encounter, each containing one of several active components. The duration of each selected interval was imposed to be a multiple of the planetary rotation period (9 hours and 55.5 min, corresponding to about four hundred 90-s spectra) in order not to bias averages over periodic emissions. 21 intervals with duration of 1 to 9 periods were selected between 2000/10/06 and 2001/03/19.

[45] 3. Determination of the typical spectral range of each component (cf. Table 1) from average spectra over each selected time interval.

[46] 4. For each component, in the intervals where it is present (≤21), we computed spectra of 50% and 1% occurrence levels (i.e., at each frequency the flux density normalized to a distance of 1 AU exceeded 50% and 1% of the time, respectively). Spectra for 50% occurrence levels are very close to average spectra but less sensitive to extreme (possibly spurious) values. Spectra for 1% occurrence are representative of peak values.

[47] The corresponding spectra are displayed on Figures 7a and 7b. Plots for individual intervals are displayed in solid lightface lines (except nKOM, which is dashed). Boldface

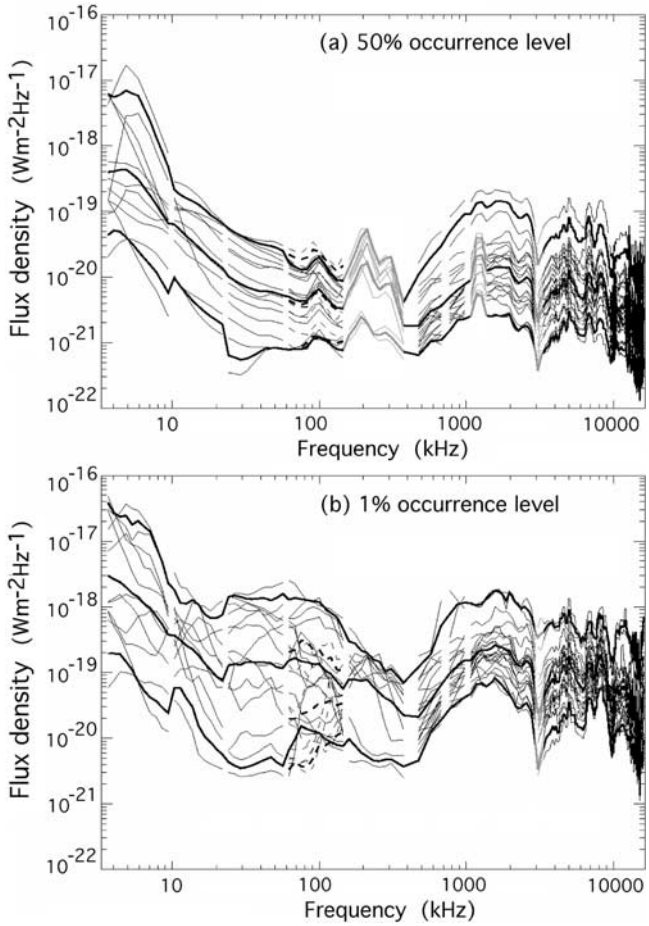


**Figure 7.** Individual spectra of Jovian radio components computed over 21 selected time intervals during which one or several components is present (lightface solid lines, except nKOM, which is shown by dashed lines). (a) Flux density level (normalized to a distance of 1 AU) exceeded 50% of the time. Boldface lines represent the average and extreme spectra of this set of curves. They can be interpreted as the average flux density level in periods of weak/medium/strong activity. (b) Flux density level (normalized to a distance of 1 AU) exceeded 1% of the time. Boldface lines represent the average and extreme spectra of this set of curves. They can be interpreted as the peak flux density level in periods of weak/medium/strong activity. Interference-dominated ranges appear in light gray.

lines represent the average and extreme spectra of the sets of curves. They can be interpreted on Figure 7a as the average flux density level in periods of weak/medium/strong activity and on Figure 7b as the peak level in periods of weak/medium/strong activity.

[48] Quasi-permanent spacecraft interference at 200 and 300 kHz (harmonics of spacecraft converters operating at 50 kHz) pollute Figure 7a, as well as an interference around 1.25 MHz in monopole mode. The dip at about 3 MHz comes from the permanent interference that pollutes the background spectrum determination of Figure 4b and makes measurements in this range not reliable in monopole mode. These spectral regions are displayed in light gray in order to emphasize the poor quality of measurements in these ranges. Pollution by interference is marginal in dipole mode because measurement of a differential voltage between two monopoles cancels out most of the spacecraft interference, but dipole measurements represent only 5.5% of the total. The interference at 200, 300, and 1250 kHz are less important in Figure 7b because they have a relatively steady level and thus do not show up in peak levels.

[49] Analysis of Figures 7a and 7b allows us to determine reliably and with reasonable accuracy the typical spectral range of each component (Table 1):

[50] 1. QP bursts cover a variable band between <3.5 and ~23 kHz. The band below 10 kHz is favored when the magnetosphere is dilated with little radio activity at high frequencies (HOM and DAM auroral components), while the band above 10 kHz corresponds to active periods with a compressed magnetosphere and thus a higher magnetosheath plasma frequency which explains the low-frequency cutoff of QP bursts observed from outside the magnetosphere (see *Hospodarsky et al.* [2004] for a comparison of Cassini and Galileo observations of QP bursts). QP bursts emission sometimes reaches frequencies larger than 23 kHz [see e.g., *MacDowall et al.*, 1993] but at these frequencies they are no more spread by propagation. It seems that Cassini did not detect any QP burst above ~50 kHz. A detailed study will be the subject of a future paper.

[51] 2. Here bKOM covers most of the time the range from 20 to 100 kHz. It extends occasionally up to ~400 kHz. It appears to be much more sporadic than the other components (see section 4.4), and almost absent on the 50% occurrence level spectrum (Figure 7a).

[52] 3. The subspectral range from 60 to 160 kHz is that of nKOM, probably generated at or near the plasma frequency at plasma inhomogeneities in the Io torus [*Reiner et al.*, 1993]. Here nKOM is much less sporadic than bKOM and thus easily discernible from it on dynamic spectra, although they cover a common spectral range.

[53] 4. HOM spectrum starts above ~400 kHz (although it may occasionally be detected down to 200 kHz and very rarely below that). It merges at about 3 MHz with the auroral (non-Io-)DAM emission. HOM and non-Io-DAM appear quasi continuously in the Jovian low-frequency spectrum. Spectral range boundaries are of course not sharp limits and the corresponding components may sometimes exceed their typical spectral range.

[54] On Figure 8 we derive a reference Jovian low-frequency radio spectrum (or rather three reference spectra) built from the measurements of Figures 7a and 7b. Flux densities are normalized to a source distance of 1 astronomical unit (AU = $1.5 \times 10^{11}$ m).

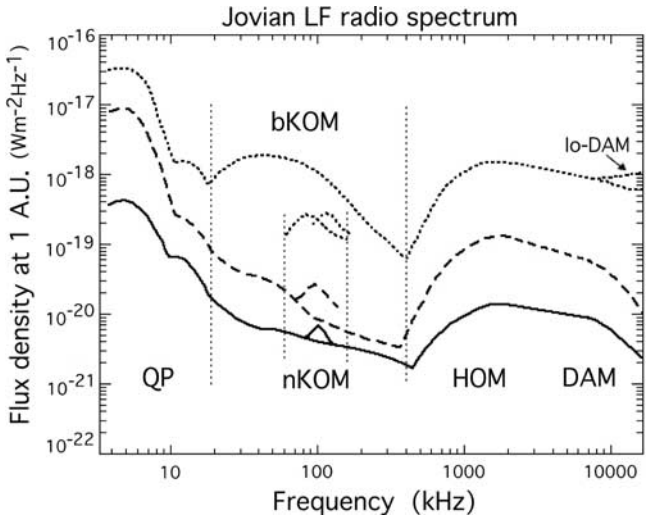


**Figure 8.** Jovian low-frequency radio spectra built from the Figures 7a and 7b. Flux densities are normalized to a distance source-observer of 1 AU. Solid curve represents the typical rotation-averaged spectrum (when corresponding emission is present). Dashed curve represents rotation-averaged spectrum at times of intense activity. Dotted curve represents the peak intensities detected during such active periods. Intense nKOM may be observed with a slightly variable spectral range. Dotted vertical lines delimit component spectral ranges (see Table 1).

[55] The solid line represents the typical spectrum averaged over one (or several) Jovian rotation as detected when the corresponding emission is present (which is almost always the case for HOM and non-Io-DAM but depends more on long-term activity for the other components). It is thus the average intensity that you may expect to detect at any random time. The dashed line corresponds to the spectrum averaged over one Jovian rotation detected when the corresponding emission is particularly strong, due to high solar wind pressure or another effect. The dotted line represent the peak intensities detected during such active periods.

[56] This spectrum reveals several facts:

[57] 1. QP bursts appears as the most intense Jovian radio component (by more than an order of magnitude). Taking into account the fact that its spectrum is superimposed to the permanent background of quasi-thermal noise, photoelectron noise, etc., increasing as $f^{-1}$ to $f^{-2}$ toward very low frequencies, the flux density attributed to QP bursts in the bottom curve of Figure 8 should be lowered by about 20%, which does not change the above conclusions.

[58] 2. Here nKOM is a low-intensity, low-power component whose flux density rarely exceeds $10^{-19}$ $Wm^{-2}$ $Hz^{-1}$.

[59] 3. Here bKOM is so sporadic that it may occasionally exceed HOM and DAM intensities.

[60] 4. HOM is generally more intense than DAM. The peak of the HOM-DAM spectrum lies between 1 and 2 MHz and not about 10 MHz as previously thought (see section 4.3 below). The DAM spectrum decreases steeply above 10 MHz.

[61] 5. Io-DAM is less frequent than non-Io-DAM but more intense above 8 MHz. Its peak value is comparable to that of HOM (but it is of course more powerful due to larger bandwidth) (cf. section 4.4). The disappearance of Io-DAM below ~2 MHz (explained by *Zarka et al.* [2001a]) combines to the HOM-DAM spectrum to form the local minimum about 8 MHz in the peak spectrum. Additional details can be inferred from Figures 7a and 7b, as, e.g., peak values for medium activity periods that appear comparable to rotation-averaged intensities during active periods, except for bKOM, whose sporadicity is exceptionally high.

### 4.3. Comparison With Previous Spectrum Measurements

[62] The first spectrum of Jovian low-frequency radio components was published by *Carr et al.* [1983, Figure 7.1]. It only includes bKOM, HOM, and DAM components and corresponds to long-term averaging. Comparison with our results shows that the bKOM and HOM spectrum of Carr et al., after normalization to an observer's distance of 1 AU, falls between the solid and dashed curves of Figure 8 and corresponds thus to long-term averages over moderate to high activity periods. However, the huge DAM peak that appears in the work of Carr et al. at 10 MHz does not exist in calibrated Cassini data. Its level at 10 MHz is close to our peak spectrum of Figure 8. We interpret its presence in the work of *Carr et al.* [1983] as a result of (1) inadequate correction of the resonance of the Voyager antenna system [see *Ortega-Molina and Daigne*, 1984], (2) poor intercalibration between ground-based and spacecraft measurements, (3) computation of the spectrum about 10 MHz over a selection of intense decameter bursts, or a combination of several of these factors.

[63] The more recent version of this spectrum computed by *Zarka* [1992] from averages over a few days of Voyager data during high activity of Jovian radiosources is consistent with our dashed curve of Figure 8 (corresponding to long-term averages over active periods) within the ±3 dB accuracy estimated in that paper. The slightly different overall spectral shapes can be attributed to occurrence of intense Io-DAM and bKOM during the averaging interval used in the work of *Zarka* [1992]. This spectrum was completed by nKOM and QP spectra by *Zarka* [2000], which also reveal consistent levels with our Figure 8 (especially with the lower, solid curve in the case of QP, which suggests that the Cassini postencounter leg was perhaps a period of especially powerful QP bursts activity).

[64] The spectra of bKOM + HOM computed from long-term averages of Ulysses radio data (restricted to frequencies below 940 kHz) in the work of *Zarka et al.* [2001a] is in good agreement with our Figure 8, especially concerning the high-frequency limit of bKOM and the low-frequency limit of HOM. Flux densities of QP bursts derived from Ulysses measurements [*MacDowall et al.*, 1993], when normalized to 1 AU distance, tend to be significantly weaker than our spectrum of Figure 8, but their overall power (estimated to $10^{7-8}$ Watts by MacDowall et al.) is consistent with our determinations in the band ~10–23 kHz as discussed below.

### 4.4. Sporadicity

[65] The sporadicity or fluctuation level of each component may be easily deduced from the plots of Figures 7a and 7b as the ratio of 1% to 50% occurrence levels for each component and each selected time period. It is thus the ratio from peak to average values within a rotation or a series of rotations. The corresponding curves are plotted on Figure 9.

[66] As expected, sporadicity of bKOM is highest with peak values up to 100–200 times larger than average ones. By contrast, QP bursts and nKOM display a fluctuation level under ~10. Its origin is different for these two emissions: nKOM appears intrinsically smooth, while QP bursts are bursty at their highest-frequency end (above 20–30 kHz in Cassini data) but they are smoothed out by propagation at lower frequencies. HOM and DAM have a level of fluctuations of a few tens, consistent with Figures 7a, 7b, and 8. The higher values at the HF end are probably not reliable and partly due to the fluctuations of the background noise spectrum in monopole mode (cf. Figure 4b).

### 4.5. Beaming

[67] Determination of the beaming of a radio component is best performed using simultaneous observations by two separated observers. This was done for HOM and DAM components observed by Cassini and Wind [*Kaiser et al.*, 2000], as well as for QP bursts observed by Cassini and Galileo [*Hospodarsky et al.*, 2004]. However, statistical information about the beaming of Jovian radio components whose source and beam rotate with the planetary field like a lighthouse may also be derived by comparing the emission intensity integrated over the beam to that averaged over the complete rotation. Practically, the former quantity is estimated at each frequency as the integrated tail of the distribution of intensities (S) at that frequency above a given threshold ($S_o$)

$$\frac{\int_{So}^{\infty} S \times N(S) \times dS}{\int_{So}^{\infty} N(S) \times dS}, \tag{7}$$

where N(S) is the distribution of intensities. The threshold should be selected to delimitate measurements containing emission from the corresponding component from measurements containing no emission. Examination of histograms of intensity distributions for the various components suggests that this threshold lies between the 10% and 1% occurrence levels.

[68] Figures 10a and 10b display the corresponding ratios $(S_{10\%}/\langle S\rangle) \times 360^\circ$ and $(S_{1\%}/\langle S\rangle) \times 360^\circ$, respectively. Boldface lines are the average values of the results for the 21 time intervals studied, and lightface lines delimit the minimum and maximum value of this ratio at each frequency. Interference-dominated ranges again appear in light gray. These curves actually correspond to the one-dimensional beaming of each radio component convoluted with the longitudinal extent of its source (we call this quantity "overall beaming" in the following). They provide an information on the instantaneous beaming pattern of each component which is less accurate than that derived from stereoscopic measurements, but this information is nevertheless crucial for studying the energetics of the corresponding emissions, as shown in the next section.

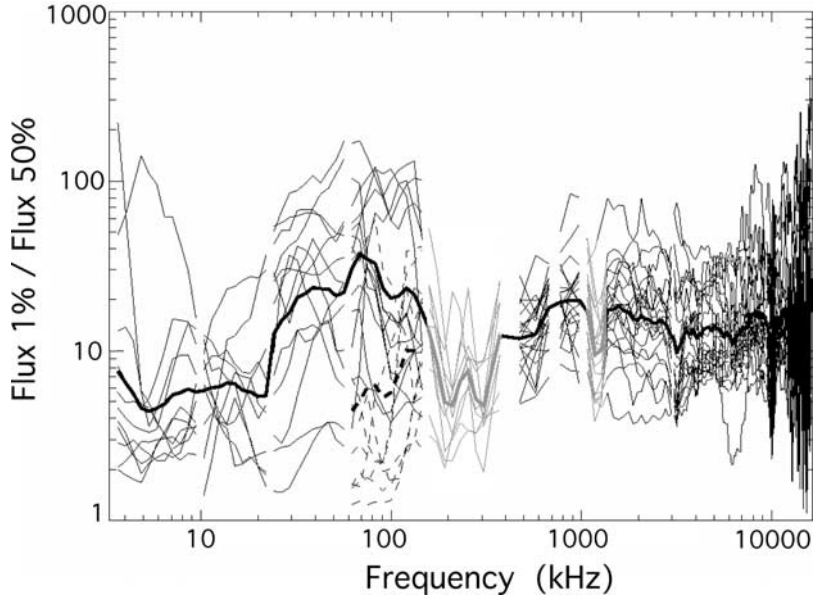


**Figure 9.** Ratio of peak to average values within a rotation or a series of rotations, as a function of frequency (derived as the ratio of 1% to 50% intensity levels for the 21 time intervals of Figures 7a and 7b). Boldface line is the average sporadicity of Jovian radio emissions as a function of frequency. Interference-dominated ranges appear in light gray.

[69] We find that nKOM has a broad overall beaming, typically about 100–150°. The nKOM sources emit broad filled cones of radio emission, as already deduced from Ulysses observations [*Stone et al.*, 1992]. The overall beaming of auroral components (bKOM, HOM, DAM) is much narrower, typically 30° ± 10° for HOM and DAM and 35° ± 15° for bKOM (as derived from the boldface lines of Figures 10a and 10b, with possible large fluctuations around these values). *Kaiser et al.* [2000] found an instantaneous beaming about 1°–2° for the width of the Io-DAM hollow conical beam and >5° for HOM. For comparison with our results, these values should be multiplied by 2 for taking into account the two sides of the cone intersected by a fixed observed during one Jovian rotation. The remaining differences are indicative of the longitudinal extents of the sources of these components. Those appear similar, i.e., 17°–37° for DAM and <10°–30° for HOM (again with large fluctuations as shown in Figure 10).

### 4.6. Power

[70] The power emitted by each Jovian low-frequency radio component may be deduced from the above results displayed in Figures 8 and 10. The average power ⟨P⟩ of a given component can be written

$$\langle P \rangle = \Omega R^2 \int_{f\,\min}^{f\,\max} S(f) \times df, \qquad (8)$$

where S is its flux density at 1 AU, R = 1 AU, [$f_{min}$, $f_{max}$] is its typical emission bandwidth, and Ω is the solid angle of the overall beam (i.e., convoluted with the source extent). Table 2 summarizes the average and peak powers of all studied Jovian radio components as deduced from the three spectra of Figure 8. Details are provided separately on low-frequency (LF) and high-frequency (HF) parts of QP, bKOM, and HOM for comparison with previous results. An empirical background has been subtracted below 200 kHz (where no galactic background is available). Beaming solid angles have been derived as explained in the notes.

[71] The results in Table 2 confirm and refine earlier published values [see, e.g., *MacDowall et al.*, 1993; *Zarka*, 1992, 1998]. They also confirm the low power and smoothness of nKOM (comparing average and peak values), the high sporadicity of bKOM, and the fact that DAM is the most powerful Jovian radio component (the tabulated value should be multiplied by ∼2 for taking into account the total band of DAM, up to 40 MHz). These values are crucial inputs for scaling laws relating output radio power to incident (kinetic or magnetic) solar wind power such as in the work of *Desch and Kaiser* [1984] or *Zarka et al.* [2001b].

[72] For Io-DAM, the low duty cycle of observed emissions makes less meaningful long-term averages. Averages over high activity periods are about $10^{10}$ W (with a beaming solid angle ∼0.16 sr [cf. *Kaiser et al.*, 2000; *Queinnec and Zarka*, 2001]) and peak values one order of magnitude larger.

## 5. Comparison With Ground-Based Observations

[73] Our calibration procedure also allows us to compare Cassini measurements of the Jovian radio spectrum to ground-based measurements performed, e.g., in Nançay, above the ionospheric cutoff (10–15 MHz). Systematic observations of Jupiter are performed at the Nançay decameter array [*Boischot et al.*, 1980; *Lecacheux*, 2000]

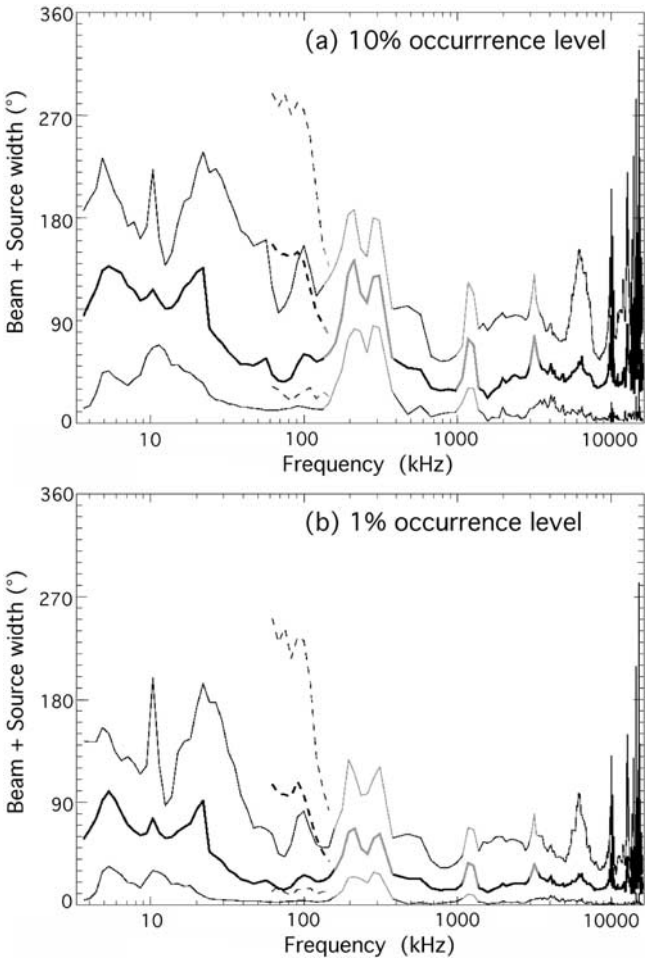


**Figure 10.** Estimates of the "overall beaming" (instantaneous beaming convoluted with the longitudinal source extent) of Jovian radio emissions as a function of frequency. It is derived by comparing the emission intensity integrated over the beam (in practice, the integrated tail of the distribution of intensities above a given threshold) to that averaged over the complete rotation. Figure 10a is an upper limit of the overall beaming corresponding to a threshold at the level exceeded 10% of the time. Figure 10b is a lower limit at the 1% occurrence level. Computation was done for the 21 time intervals of Figures 7a and 7b but for clarity only average and extreme values are displayed on Figures 10a and 10b. Interference-dominated ranges appear in light gray.

with a swept-frequency spectrum analyzer, up to 8 hours per day (meridian transit ±4 hours), between 10 and 40 MHz. Spectral resolution is 75 kHz and channel width 30 kHz. One spectrum is recorded every 0.5 s (corresponding to $\sim$1 ms integration time per channel), alternatively in left-hand and right-hand circular polarization. The effective area of the instrument, $\sim$3500 $m^2$ at 25 MHz, ensures a sensitivity of $\sim 10^{-22}$ $Wm^{-2}$ $Hz^{-1}$, comparable to that of Cassini-RPWS (cf. Figure 7a). The receiver has an 80 dB dynamic range, and the gain of the system is nearly independent of frequency in the range 10–40 MHz, providing reliable flux measurements.

[74] We have searched for a few cases when the same Jovian decameter sources are observed by Cassini and in Nançay. Although the sensitivity threshold in Nançay is comparable to that of Cassini, such coincidences are not very common because (1) the duty cycle of Nançay observations is $\leq$1/3, (2) man-made interference often saturates the range below 15–20 MHz, preventing detection of Jovian radio emissions at these frequencies, and (3) except for the rare opportunities when Earth, Cassini, and Jupiter were aligned together, there is a delay between the illumination of two separated observers by the Jovian lighthouse-like DAM beam: this delay is 1.7 min per degree of separation for non-Io-DAM emissions rotating with a $\sim$10 hour period but 7 min/degree for Io-DAM emissions rotating with Io's orbital motion of period $\sim$42.5 hours. During this delay, the variable Jovian emissions may turn off (or on) and thus be observed by one only of the two observers.

[75] We were able to find a few favorable cases, one of which is illustrated in Figure 11. Near the beginning of 2000/11/28 (DOY 333), several Jovian DAM bursts of a few minutes duration each were observed in Nançay below 16 MHz (top). Similar bursts were detected by Cassini RPWS (bottom) about 1 hour earlier. The corresponding geometry Cassini-Jupiter-Earth at that time is sketched in Figure 12. The angle Cassini-Jupiter-Earth was $\sim$13.4°, corresponding to a delay of 22.1 min between observation of the non-Io-DAM beam by Cassini and then from Earth. The difference in light travel time was 33.2 min, hence a total delay of 55.3 min (or 2 hours 6 min for Io-DAM).

[76] In order to compare Cassini and Nançay observations, a frequency-dependent background (including the galactic noise plus instrumental noise and the steady part of interference) was subtracted from Nançay data. This background was computed as in section 2.4 (mode of the distribution of intensities at each frequency). The top panel of Figure 11 displays the Nançay data after background subtraction.

[77] Figure 13a displays the time variations of the flux density measured by Cassini and in Nançay, averaged over the range 12–16 MHz. In the case of Nançay data, only those channels not dominated by interference were taken into account within that band. Time is UT at Earth: Cassini spacecraft event time has been shifted by +55.3 min. This plot shows that correlated emissions are observed by Cassini and in Nançay between 2000/11/27 2330 and 2000/11/28 0107. The levels of emission peaks are very similar for both observers, well within a factor of two, in spite of the $\sim$1 hour time shift between actual observations. This good correlation bring support to the facts that (1) Cassini/RPWS-HFR calibrated fluxes are accurate to better than a factor of two; (2) The emission observed by Cassini and Nançay on 2000/11/28 is non-Io-DAM, rotating with Jupiter; this conclusion is confirmed by the position of the observer in a diagram CML (Central Meridian Longitude is observer's Jovian longitude) Io phase (orbital position relative to the observer-Jupiter line), which corresponds to Io-independent geometry of observation [see, e.g., *Carr et al.*, 1983].

[78] The larger fluctuations affecting Nançay data may be attributed to scintillation through ionospheric inhomo-

**Table 2.** Average and Peak Powers of Jovian Radio Components

| Component | Spectral Range, kHz | Beam Solid Angle Ω, sr | Average Power, W | Average Power (High Activity), W | Peak Power, W |
|---|---|---|---|---|---|
| QP (LF) | 3.5–10 | $2\pi$ | $2.3 \times 10^8$ | $4.5 \times 10^9$ | $5.5 \times 10^9$ |
| QP (HF) | 10–23 | $2\pi$ | $5.6 \times 10^7$ | $2.9 \times 10^8$ | $7.0 \times 10^8$ |
| QP (total) | 3.5–23 | $2\pi$[a] | $2.9 \times 10^8$ | $4.8 \times 10^9$ | $6.2 \times 10^9$ |
| nKOM | 60–160 | 4.8[b] | $5.0 \times 10^7$ | $2.4 \times 10^8$ | $7.7 \times 10^8$ |
| bKOM (LF) | 23–200 | 1.9 | $7.1 \times 10^7$ | $3.0 \times 10^8$ | $7.2 \times 10^9$ |
| bKOM (HF) | 200–400 | 1.9 | $1.0 \times 10^8$ | $1.8 \times 10^8$ | $1.9 \times 10^9$ |
| bKOM (total) | 23–400 | 1.9[c] | $1.7 \times 10^8$ | $4.8 \times 10^8$ | $9.1 \times 10^9$ |
| HOM (LF) | 400–1000 | 1.6 | $5.1 \times 10^8$ | $4.0 \times 10^9$ | $1.5 \times 10^{10}$ |
| HOM (HF) | 1000–3000 | 1.6 | $3.8 \times 10^9$ | $3.5 \times 10^{10}$ | $1.2 \times 10^{11}$ |
| HOM (total) | 400–3000 | 1.6[c] | $4.3 \times 10^9$ | $3.9 \times 10^{10}$ | $1.4 \times 10^{11}$ |
| DAM | 3000–16000 | 1.6[c] | $1.3 \times 10^{10}$ | $8.2 \times 10^{10}$ | $4.5 \times 10^{11}$ |

[a]See, e.g., *Hospodarsky et al.* [2004] (QP bursts are detected mostly from Jupiter's dusk side) and Figures 10a and 10b.
[b]$\Omega = \theta^2$ with $\theta = 125°$ (average of two values of Figures 10a and 10b).
[c]Assuming a hollow cone of half-angle aperture ~75° and thickness = δθ [*Queinnec and Zarka*, 1998; *Kaiser et al.*, 2000], we obtain: $\Omega = \int_{75-\delta\theta/2}^{75+\delta\theta/2} 2\pi \sin(\theta) d\theta$, where $\delta\theta = 17.5°$ for bKOM and 15° HOM and DAM (half the mean value between Figures 10a and 10b).

geneities because the observing frequency is close to the maximum ionospheric plasma frequency. The third large emission peak about 1.3 hour on Figure 13a was observed by Cassini but not detected in Nançay. This is probably due to the corresponding source having turned off during the 1-hour delay required for the beam to rotate from the Jupiter-Cassini direction to the Jupiter-Earth direction. This source may also be Io-DAM, which would imply in that case a >2-hour delay during which the Nançay observations have ceased.

[79] Figure 13b compares the spectra measured in Nançay between 0020 and 0110 and by Cassini 55 min earlier. Again, the agreement between the measured fluxes is excellent apart from the channels heavily polluted by interference, better than a factor of two. This confirms the accuracy of our calibration and allows one to combine Cassini and ground-based measurements to obtain composite spectra between 3.5 kHz and ≥40 MHz.

## 6. Conclusions

[80] By applying the calibration method developed by *Dulk et al.* [2001] to the data from the Cassini/RPWS High-Frequency Receiver, we have derived absolute flux density

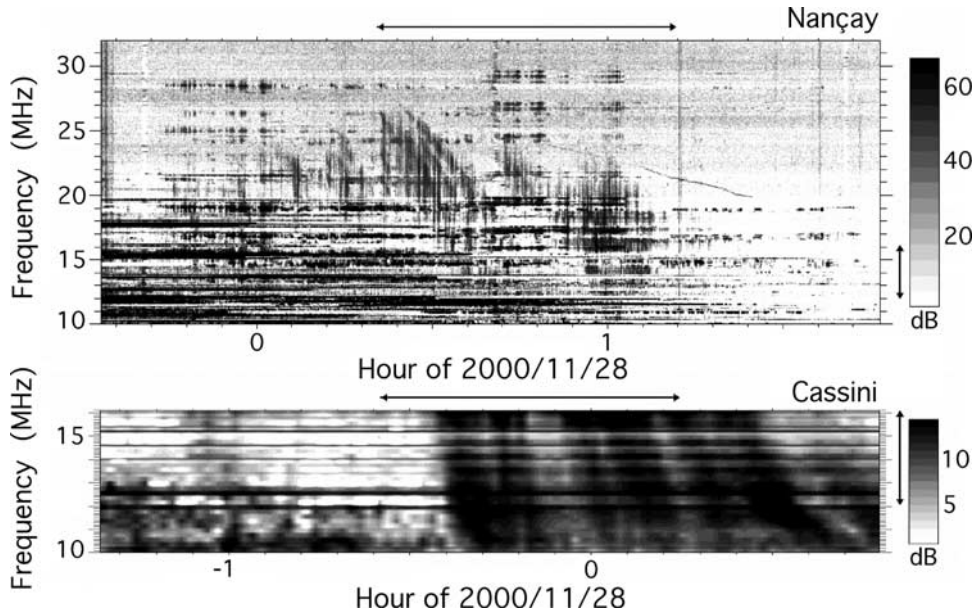


**Figure 11.** Example of Jovian DAM emission observed quasi-simultaneously by Cassini (bottom panel) and on the ground (in Nançay, France in the upper panel), on 2000/11/28 (DOY 333). The two panels have been aligned with a time shift of 55.3 min, corresponding to the delay expected for a radiosource rotating with Jupiter. The large bursts at 0.6 and 1.0 hour (Nançay time) correspond well to Cassini observations. Horizontal lines in both panels are interference (man-made or spacecraft-generated). A background has been subtracted in both cases. Vertical arrows delimit the spectral range over which integration has been performed to obtain the time profile of Figure 13a. Horizontal arrows delimit the time intervals over which integration has been performed to obtain the spectrum of Figure 13b.

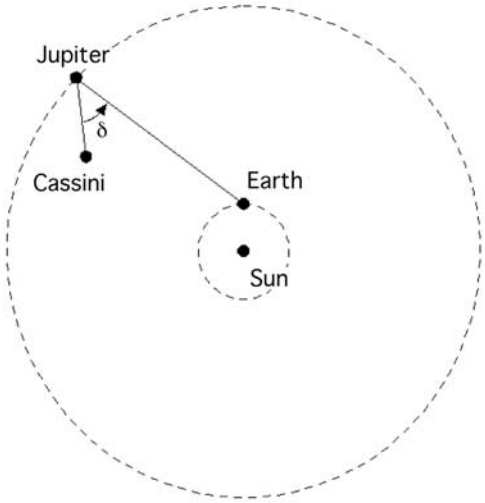


**Figure 12.** Cassini-Jupiter-Earth geometry at the time of the observations of Figure 11. Distance from Cassini to Jupiter was 0.21 AU, while distance from Earth to Jupiter was 4.2 AU, hence a light travel time delay of 33.2 min. Cassini-Jupiter-Earth angle was $\delta \sim 13.4°$, corresponding to a delay of 22.1 min between illumination of Cassini and Earth by a beam rotating with Jupiter (93 min for a beam rotating with Io).

measurements of six components of the Jovian low-frequency radio spectrum over the full frequency range of the instrument (3.5 kHz to 16.1 MHz). The achieved accuracy is estimated to be better than 50%, i.e., much less

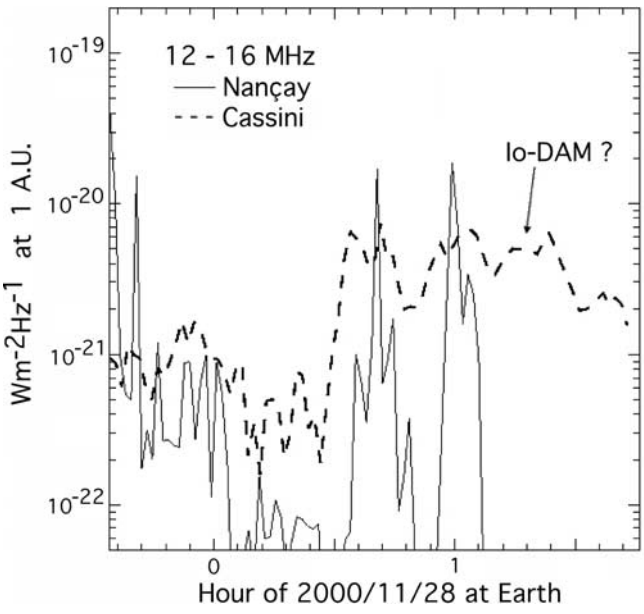


**Figure 13a.** Time variations of the flux density measured by Cassini and in Nançay, averaged over the range 12–16 MHz (arrowed in Figure 11). In the case of Nançay data, only those channels not dominated by interference were taken into account within that band. Time is UT at Earth: Cassini spacecraft event time has been shifted by +55.3 min.

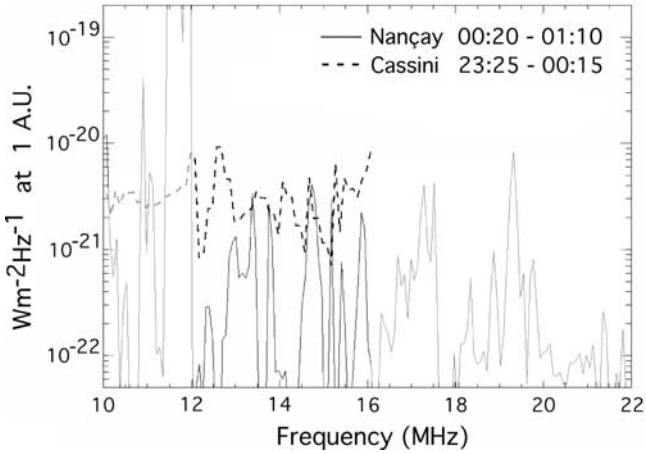


**Figure 13b.** Comparison of the spectra measured in Nançay between 0020 and 0110 and by Cassini 55.3 min earlier (time intervals arrowed in Figure 11). The common spectral range is emphasized. A broad intense interference pollutes Nançay data between ~11.5 and 12 MHz.

than the intrinsic variations of the flux densities of these radiosources. It is mainly limited by the accuracy of the model used for the radio galactic background (equation (2) and Figure 1).

[81] Let us remark here that although the galactic background spectrum is rather weak (within 10 dB of the lowest measured noise levels below ~5 MHz) (see Figures 4a and 4b), it is well adapted to the calibration of RPWS-HFR data even at the highest detected levels. This is due to the fact that the instrument has a linear response over a dynamic range of ≥70 dB [see *Manning*, 1999], while the most intense emissions detected during the Jupiter flyby (Figures 7b and 8) are no more than 50–55 dB above the galactic background (Figure 1). In-flight internal HFR calibrations allow one to check periodically that the detected signals remain within the linear range of the instrument response. Instrumental parameters such as the antennas' effective lengths and base capacitance are constrained in the calibration process, through comparison of the results obtained in the short dipole approximation with calibration using the galactic background spectrum.

[82] A data set of 6 months centered on the Cassini-Jupiter flyby is then computed, allowing long-term studies of Jovian radio components on the basis of quasi-continuous, calibrated observations. We derive thus the average Jovian radio spectrum between 3.5 and 16.1 MHz corresponding to average and high level of activity of each radio component, as well as the peak radio spectrum for each component (Figure 8). These different spectra correspond to well-defined conditions of observation and averaging and can serve as a reference for comparison with earlier or future observations (suggesting for example that the large peak at 10 MHz in the Jovian radio spectrum from *Carr et al.* [1983] is not real). From the range of fluctuations of the intensity of each component, we infer a measure of its sporadicity and estimate its overall beaming (instantaneous beaming convoluted with the longitudinal source extent). The latter is used at

determining the power emitted by each component (Table 2). We have also briefly discussed long-term variations of the various Jovian low-frequency radio components, but the systematic study of modulations and long-term temporal variations of Jovian radio components (due to rotation, Io, solar wind control) will be the subject of a further paper.

[83] Finally, our calibration procedure also allows us to compare Cassini measurements with ground-based measurements performed in Nançay above the ionospheric cutoff (10–15 MHz). The matching is again better than a factor of two. Composite spectra covering the range from 3.5 kHz to $\geq$40 MHz can thus be obtained. This calibration procedure will be used to derive absolute flux measurements during the Saturn tour. One can for example imagine comparing Cassini measurements of Saturn's lightning with ground-based observation of the same events [*Zarka et al.*, 2004].

[84] **Acknowledgments.** We acknowledge the support from the Cassini-RPWS team, and especially its P.I. Don Gurnett, Terry Averkamp and Don Kirchner from the Iowa technical staff, and Pierre Fédou and Nicole Letourneur from the Meudon technical staff. PZ and BC thank Laurent Denis (Nançay Decameter Array), Solène Blancho, and Michel Nuevo (students) for their help with Nançay data, and Renée Prangé for many constructive discussions. The Nançay Radio Observatory/Unité Scientifique de Nançay of the Observatoire de Paris (USR B704-CNRS) acknowledges the financial support of the Conseil Régional of the Région Centre in France. Cassini-RPWS activities at LESIA are supported by the French CNES (Centre National d'Études Spatiales). The research at The University of Iowa was supported by NASA through contract 961152 through the Jet Propulsion Laboratory. Last but not least, PZ would like to express his gratitude to the late "Bob" Manning, who was an esteemed colleague and a friend.

[85] Arthur Richmond thanks Michael Kaiser and another reviewer for their assistance in evaluating this paper.

## References

Boischot, A., C. Rosolen, M. G. Aubier, G. Daigne, F. Genova, Y. Leblanc, A. Lecacheux, J. de la Noë, and B. M. Pedersen (1980), A new high-gain broadband steerable array to study Jovian decametric emissions, *Icarus*, *43*, 399–407.

Bougeret, J.-L., et al. (1998), A shock associated (SA) radio event and related phenomena observed from the base of the solar corona to 1 AU, *Geophys. Res. Lett.*, *25*(14), 2513–2516. (Correction, *Geophys. Res. Lett., 25*, 4103, 1998.)

Carr, T. D., M. D. Desch, and J. K. Alexander (1983), Phenomenology of magnetospheric radio emissions, in *Physics of the Jovian Magnetosphere*, edited by A. J. Dessler, pp. 226–284, Cambridge Univ. Press, New York.

Desch, M. D. (1994), Jupiter radio bursts and particle acceleration, *Astrophys. J. Suppl. Ser.*, *90*, 541–546.

Desch, M. D., and M. L. Kaiser (1984), Predictions for Uranus from a radiometric Bode's law, *Nature*, *310*, 755–757.

Dulk, G. A., W. C. Erickson, R. Manning, and J.-L. Bougeret (2001), Calibration of low-frequency radio telescopes using the galactic background radiation, *Astron. Astrophys.*, *365*, 294–300.

Gurnett, D. A., P. Zarka, R. Manning, W. S. Kurth, G. B. Hospodarsky, T. F. Averkamp, M. L. Kaiser, and W. M. Farrell (2001), Non-detection at Venus of high-frequency radio signals characteristic of terrestrial lightning, *Nature*, *409*, 313–315.

Gurnett, D. A., et al. (2002), Control of Jupiter's radio emission and aurorae by the solar wind, *Nature*, *415*, 985–987.

Gurnett, D. A., et al. (2004), The Cassini radio and plasma wave investigation, *Space Sci. Rev.*, in press.

Hospodarsky, G. B., W. S. Kurth, B. Cecconi, D. A. Gurnett, M. L. Kaiser, M. D. Desch, and P. Zarka (2004), Simultaneous observations of jovian quasi-periodic radio emissions by the Galileo and Cassini spacecraft, *J. Geophys. Res.*, *109*, A09S07, doi:10.1029/2003JA010263.

Kaiser, M. L. (1998), Jovian and terrestrial low-frequency radio bursts: Possible cause of anomalous continuum, *J. Geophys. Res.*, *103*, 19,993–20,000.

Kaiser, M. L., M. D. Desch, and W. M. Farrell (1993), Clock-like behavior of Jovian continuum radiation, *Planet. Space Sci.*, *41*, 1073–1077.

Kaiser, M. L., P. Zarka, W. S. Kurth, G. B. Hospodarsky, and D. A. Gurnett (2000), Cassini and Wind stereoscopic observations of Jovian non-thermal radio emissions: Measurements of beamwidths, *J. Geophys. Res.*, *105*, 16,053–16,062.

Kurth, W. S. (1992), Continuum radiation in planetary magnetospheres, in *Planetary Radio Emissions III*, edited by H. O. Rucker, S. J. Bauer, and M. L. Kaiser, pp. 329–350, Austrian Acad. Sci. Press, Vienna, Austria.

Kurth, W. S., G. B. Hospodarsky, D. A. Gurnett, M. L. Kaiser, J.-E. Wahlund, A. Roux, P. Canu, P. Zarka, and Y. Tokarev (2001), An overview of observations by the Cassini Radio and Plasma Wave investigation at Earth, *J. Geophys. Res.*, *106*, 30,239–30,252.

Ladreiter, H. P., P. Zarka, and A. Lecacheux (1994), Direction-finding study of Jovian Hectometric and broadband Kilometric radio emissions: Evidence for their auroral origin, *Planet. Space Sci.*, *42*, 919–931.

Ladreiter, H. P., P. Zarka, A. Lecacheux, W. Macher, H. O. Rucker, R. Manning, D. A. Gurnett, and W. S. Kurth (1995), Analysis of electromagnetic wave direction-finding performed by spaceborne antennas using singular value decomposition techniques, *Radio Sci.*, *30*, 1699–1712.

Lecacheux, A. (2000), The Nançay decameter array: A useful step towards giant, new generation radio telescopes for long wavelength radio astronomy, in *Radio Astronomy at Long Wavelengths*, *Geophys. Monogr. Ser.*, vol. 119, edited by R. G. Stone et al., pp. 321–328, AGU, Washington, D. C.

Lecacheux, A., B. M. Pedersen, P. Zarka, M. G. Aubier, M. D. Desch, W. M. Farrell, M. L. Kaiser, R. J. MacDowall, and R. G. Stone (1992), In ecliptic observations of Jovian radio emissions by Ulysses: Comparison with Voyager results, *Geophys. Res. Lett.*, *19*, 1307–1310.

Louarn, P., et al. (1998), A study of the large-scale dynamics of the Jovian magnetosphere using the Galileo plasma wave experiment, *Geophys. Res. Lett.*, *25*, 2905–2908.

MacDowall, R. J., M. L. Kaiser, M. D. Desch, W. M. Farrell, R. A. Hess, and R. G. Stone (1993), Quasiperiodic Jovian radio bursts: Observations from the Ulysses Radio and Plasma Wave experiment, *Planet. Space Sci.*, *41*, 1059–1072.

Manning, R. (1999), Calibration of flight model #1 of Cassini-RPWS High Frequency Receiver (HFR)/KRONOS, Int. Rep., Dep. of Space Res., Paris Observatory, Paris.

Manning, R. (2000), Instrumentation for space-based low frequency radio astronomy, in *Radio Astronomy at Long Wavelengths*, *Geophys. Monogr. Ser.*, vol. 119, edited by R. G. Stone et al., pp. 329–337, AGU, Washington, D. C.

Manning, R., and G. A. Dulk (2001), The Galactic background radiation from 0.2 to 13.8 MHz, *Astron. Astrophys.*, *372*, 663–666.

Ortega-Molina, A., and G. Daigne (1984), Polarization response of two crossed monopoles on a spacecraft, *Astron. Astrophys.*, *130*, 301–310.

Queinnec, J., and P. Zarka (1998), Io-controlled decameter arcs and Io-Jupiter interaction, *J. Geophys. Res.*, *103*, 26,649–26,666.

Queinnec, J., and P. Zarka (2001), Flux, power, energy and polarization of Jovian S-bursts, *Planet. Space Sci.*, *49*, 365–376.

Reiner, M. J., J. Fainberg, R. G. Stone, M. L. Kaiser, M. D. Desch, R. Manning, P. Zarka, and B. M. Pedersen (1993), Source characteristics of Jovian narrow-band kilometric radio emissions, *J. Geophys. Res.*, *98*, 13,163–13,176.

Robinson, P. A., and I. H. Cairns (2000), Theory of Type III and Type II Solar Radio Emissions, in *Radio Astronomy at Long Wavelengths*, *Geophys. Monogr. Ser.*, vol. 119, edited by R. G. Stone et al., pp. 37–46, AGU, Washington, D. C.

Rucker, H. O., W. Macher, R. Manning, and H. P. Ladreiter (1996), Cassini model rheometry, *Radio Sci.*, *31*, 1299–1311.

Steinberg, J.-L., C. Lacombe, P. Zarka, S. Hoang, and C. Perche (2004), Terrestrial low frequency bursts: Espace paths of radio waves through the bow shock, *Planet. Space Sci.*, in press.

Stone, R. G., et al. (1992), Ulysses Radio and Plasma wave observations in the Jupiter environment, *Science*, *257*, 1524–1531.

Vogl, D. F., et al. (2004), In-flight calibration of the Cassini Radio and Plasma Wave Science (RPWS) antenna system for direction finding and polarization measurements, *J. Geophys. Res.*, *109*, A09S17, doi:10.1029/2003JA010261.

Zarka, P. (1992), The auroral radio emissions from planetary magnetospheres: What do we know, what don't we know, what do we learn from them?, *Adv. Space Res.*, *12*, (8)99–(8)115.

Zarka, P. (1998), Auroral radio emissions at the outer planets: Observations and theories, *J. Geophys. Res.*, *103*, 20,159–20,194.

Zarka, P. (2000), Radio emissions from the planets and their moons, in *Radio Astronomy at Long Wavelengths*, *Geophys. Monogr. Ser.*,

vol. 119, edited by R. G. Stone et al., pp. 167–178, AGU, Washington, D. C.

Zarka, P. (2004), Radio and plasma waves at the outer planets, *Adv. Space Res.*, in press.

Zarka, P., J. Queinnec, and F. Crary (2001a), Low-frequency limit of Jovian radio emissions and implications on source locations and Io plasma wake, *Planet. Space Sci.*, *49*, 1137–1149.

Zarka, P., R. A. Treumann, B. P. Ryabov, and V. B. Ryabov (2001b), Magnetically-driven planetary radio emissions and applications to extrasolar planets, *Astrophys. Space Sci.*, *277*, 293–300.

Zarka, P., M. L. Kaiser, and W. S. Kurth (2004), Study of solar system planetary lightning with LOFAR, *Planet. Space Sci.*, in press.

B. Cecconi and P. Zarka, Laboratoire d'Etudes Spatiales et d'Instrumentation en Astrophysique (LESIA), Observatoire de Paris, UMR 8109 du Centre National de la Recherche Scientifique, F-92190 Meudon, France. (baptiste.cecconi@obspm.fr; philippe.zarka@obspm.fr)

W. S. Kurth, Department of Physics and Astronomy, University of Iowa, Iowa City, IA 52242, USA. (william-kurth@uiowa.edu)